The Astrophysical Journal Letters, 960:L11 (15pp), 2024 January 10 https://doi.org/10.3847/2041-8213/ad132d

Highly Significant Detection of X-Ray Polarization from the Brightest Accreting Neutron Star Sco X-1

Fabio La Monaca[1,2,3], Alessandro Di Marco[1], Juri Poutanen[4], Matteo Bachetti[5], Sara Elisa Motta[6], Alessandro Papitto[7], Maura Pilia[5], Fei Xie[1,8], Stefano Bianchi[9], Anna Bobrikova[4], Enrico Costa[1], Wei Deng[8], Ming-Yu Ge[10], Giulia Illiano[2,3,7], Shu-Mei Jia[10], Henric Krawczynski[11], Eleonora Veronica Lai[5], Kuan Liu[8], Guglielmo Mastroserio[12], Fabio Muleri[1], John Rankin[1], Paolo Soffitta[1], Alexandra Veledina[4,13], Filippo Ambrosino[7], Melania Del Santo[14], Wei Chen[8], Javier A. Garcia[15], Philip Kaaret[16], Thomas D. Russell[14], Wen-Hao Wei[8], Shuang-Nan Zhang[10], Chao Zuo[8], Zaven Arzoumanian[15], Massimo Cocchi[5], Andrea Gnarini[9], Ruben Farinelli[17], Keith Gendreau[15,18], Francesco Ursini[9], Martin C. Weisskopf[16], Silvia Zane[19], Iván Agudo[20], Lucio A. Antonelli[7,21], Luca Baldini[22,23], Wayne H. Baumgartner[16], Ronaldo Bellazzini[22], Stephen D. Bongiorno[16], Raffaella Bonino[24,25], Alessandro Brez[22], Niccolò Bucciantini[26,27,28], Fiamma Capitanio[1], Simone Castellano[22], Elisabetta Cavazzuti[29], Chien-Ting Chen[30], Stefano Ciprini[21,31], Alessandra De Rosa[1], Ettore Del Monte[1], Laura Di Gesu[29], Niccolò Di Lalla[32], Immacolata Donnarumma[29], Victor Doroshenko[33], Michal Dovčiak[34], Steven R. Ehlert[16], Teruaki Enoto[35], Yuri Evangelista[1], Sergio Fabiani[1], Riccardo Ferrazzoli[1], Shuichi Gunji[36], Kiyoshi Hayashida[37,56], Jeremy Heyl[38], Wataru Iwakiri[39], Svetlana G. Jorstad[40,41], Vladimir Karas[34], Fabian Kislat[42], Takao Kitaguchi[35], Jeffery J. Kolodziejczak[16], Luca Latronico[24], Ioannis Liodakis[16], Simone Maldera[24], Alberto Manfreda[43], Frédéric Marin[44], Andrea Marinucci[29], Alan P. Marscher[40], Herman L. Marshall[45], Francesco Massaro[24,25], Giorgio Matt[9], Ikuyuki Mitsuishi[46], Tsunefumi Mizuno[47], Michela Negro[48], Chi-Yung Ng[49], Stephen L. O'Dell[16], Nicola Omodei[32], Chiara Oppedisano[24], George G. Pavlov[50], Abel L. Peirson[32], Matteo Perri[7,21], Melissa Pesce-Rollins[22], Pierre-Olivier Petrucci[51], Andrea Possenti[5], Simonetta Puccetti[21], Brian D. Ramsey[16], Ajay Ratheesh[1], Oliver J. Roberts[30], Roger W. Romani[32], Carmelo Sgrò[22], Patrick Slane[52], Gloria Spandre[22], Douglas A. Swartz[30], Toru Tamagawa[35], Fabrizio Tavecchio[6], Roberto Taverna[53], Yuzuru Tawara[46], Allyn F. Tennant[16], Nicholas E. Thomas[16], Francesco Tombesi[2,31,54], Alessio Trois[5], Sergey S. Tsygankov[4], Roberto Turolla[19,53], Jacco Vink[55], and Kinwah Wu[19]
(IXPE Collaboration)

[1] INAF Istituto di Astrofisica e Planetologia Spaziali, Via del Fosso del Cavaliere 100, I-00133 Roma, Italy; fabio.lamonaca@inaf.it
[2] Dipartimento di Fisica, Università degli Studi di Roma "Tor Vergata," Via della Ricerca Scientifica 1, I-00133 Roma, Italy
[3] Dipartimento di Fisica, Università degli Studi di Roma "La Sapienza," Piazzale Aldo Moro 5, I-00185 Roma, Italy
[4] Department of Physics and Astronomy, 20014 University of Turku, Finland
[5] INAF Osservatorio Astronomico di Cagliari, Via della Scienza 5, I-09047 Selargius (CA), Italy
[6] INAF Osservatorio Astronomico di Brera, Via E. Bianchi 46, I-23807 Merate (LC), Italy
[7] INAF Osservatorio Astronomico di Roma, Via Frascati 33, I-00040 Monte Porzio Catone (RM), Italy
[8] Guangxi Key Laboratory for Relativistic Astrophysics, School of Physical Science and Technology, Guangxi University, Nanning 530004, People's Republic of China
[9] Dipartimento di Matematica e Fisica, Università degli Studi Roma Tre, Via della Vasca Navale 84, I-00146 Roma, Italy
[10] Key Laboratory of Particle Astrophysics, Institute of High Energy Physics, Chinese Academy of Sciences, Beijing, People's Republic of China
[11] Physics Department and McDonnell Center for the Space Sciences, Washington University in St. Louis, St. Louis, MO 63130, USA
[12] Università degli Studi di Milano, Via Celoria 16, I-20133 Milano, Italy
[13] Nordita, KTH Royal Institute of Technology and Stockholm University, Hannes Alfvéns väg 12, SE-10691 Stockholm, Sweden
[14] INAF, Istituto di Astrofisica Spaziale e Fisica Cosmica, Via U. La Malfa 153, I-90146 Palermo, Italy
[15] NASA Goddard Space Flight Center, Code 662, Greenbelt, MD 20771, USA
[16] NASA Marshall Space Flight Center, Huntsville, AL 35812, USA
[17] INAF Osservatorio di Astrofisica e Scienza dello Spazio di Bologna, Via P. Gobetti 101, I-40129 Bologna, Italy
[18] Center for Exploration and Space Studies (CRESST), NASA/GSFC, Greenbelt, MD 20771, USA
[19] Mullard Space Science Laboratory, University College London, Holmbury St Mary, Dorking, Surrey RH5 6NT, UK
[20] Instituto de Astrofísica de Andalucía—CSIC, Glorieta de la Astronomía s/n, E-18008 Granada, Spain
[21] Space Science Data Center, Agenzia Spaziale Italiana, Via del Politecnico snc, I-00133 Roma, Italy
[22] Istituto Nazionale di Fisica Nucleare, Sezione di Pisa, Largo B. Pontecorvo 3, I-56127 Pisa, Italy
[23] Dipartimento di Fisica, Università di Pisa, Largo B. Pontecorvo 3, I-56127 Pisa, Italy
[24] Istituto Nazionale di Fisica Nucleare, Sezione di Torino, Via Pietro Giuria 1, I-10125 Torino, Italy
[25] Dipartimento di Fisica, Università degli Studi di Torino, Via Pietro Giuria 1, I-10125 Torino, Italy
[26] INAF Osservatorio Astrofisico di Arcetri, Largo Enrico Fermi 5, I-50125 Firenze, Italy
[27] Dipartimento di Fisica e Astronomia, Università degli Studi di Firenze, Via Sansone 1, I-50019 Sesto Fiorentino (FI), Italy
[28] Istituto Nazionale di Fisica Nucleare, Sezione di Firenze, Via Sansone 1, I-50019 Sesto Fiorentino (FI), Italy
[29] Agenzia Spaziale Italiana, Via del Politecnico snc, I-00133 Roma, Italy
[30] Science and Technology Institute, Universities Space Research Association, Huntsville, AL 35805, USA
[31] Istituto Nazionale di Fisica Nucleare, Sezione di Roma "Tor Vergata," Via della Ricerca Scientifica 1, I-00133 Roma, Italy
[32] Department of Physics and Kavli Institute for Particle Astrophysics and Cosmology, Stanford University, Stanford, CA 94305, USA
[33] Institut für Astronomie und Astrophysik, Universität Tübingen, Sand 1, D-72076 Tübingen, Germany
[34] Astronomical Institute of the Czech Academy of Sciences, Boční II 1401/1, 14100 Praha 4, Czech Republic
[35] RIKEN Cluster for Pioneering Research, 2-1 Hirosawa, Wako, Saitama 351-0198, Japan
[36] Yamagata University, 1-4-12 Kojirakawa-machi, Yamagata-shi 990-8560, Japan
[37] Osaka University, 1-1 Yamadaoka, Suita, Osaka 565-0871, Japan

[38] University of British Columbia, Vancouver, BC V6T 1Z4, Canada
[39] International Center for Hadron Astrophysics, Chiba University, Chiba 263-8522, Japan
[40] Institute for Astrophysical Research, Boston University, 725 Commonwealth Avenue, Boston, MA 02215, USA
[41] Department of Astrophysics, St. Petersburg State University, Universitetsky pr. 28, Petrodvoretz, 198504 St. Petersburg, Russia
[42] Department of Physics and Astronomy and Space Science Center, University of New Hampshire, Durham, NH 03824, USA
[43] Istituto Nazionale di Fisica Nucleare, Sezione di Napoli, Strada Comunale Cinthia, I-80126 Napoli, Italy
[44] Université de Strasbourg, CNRS, Observatoire Astronomique de Strasbourg, UMR 7550, F-67000 Strasbourg, France
[45] MIT Kavli Institute for Astrophysics and Space Research, Massachusetts Institute of Technology, 77 Massachusetts Avenue, Cambridge, MA 02139, USA
[46] Graduate School of Science, Division of Particle and Astrophysical Science, Nagoya University, Furo-cho, Chikusa-ku, Nagoya, Aichi 464-8602, Japan
[47] Hiroshima Astrophysical Science Center, Hiroshima University, 1-3-1 Kagamiyama, Higashi-Hiroshima, Hiroshima 739-8526, Japan
[48] Department of Physics and Astronomy, Louisiana State University, Baton Rouge, LA 70803, USA
[49] Department of Physics, University of Hong Kong, Pokfulam, Hong Kong
[50] Department of Astronomy and Astrophysics, Pennsylvania State University, University Park, PA 16801, USA
[51] Université Grenoble Alpes, CNRS, IPAG, F-38000 Grenoble, France
[52] Center for Astrophysics, Harvard & Smithsonian, 60 Garden Street, Cambridge, MA 02138, USA
[53] Dipartimento di Fisica e Astronomia, Università degli Studi di Padova, Via Marzolo 8, I-35131 Padova, Italy
[54] Department of Astronomy, University of Maryland, College Park, MD 20742, USA
[55] Anton Pannekoek Institute for Astronomy & GRAPPA, University of Amsterdam, Science Park 904, 1098 XH Amsterdam, The Netherlands
Received 2023 November 10; revised 2023 November 28; accepted 2023 December 5; published 2024 January 5

Abstract

The Imaging X-ray Polarimetry Explorer measured with high significance the X-ray polarization of the brightest Z-source, Sco X-1, resulting in the nominal 2–8 keV energy band in a polarization degree of $1.0\% \pm 0.2\%$ and a polarization angle of $8^\circ \pm 6^\circ$ at a 90% confidence level. This observation was strictly simultaneous with observations performed by NICER, NuSTAR, and Insight-HXMT, which allowed for a precise characterization of its broadband spectrum from soft to hard X-rays. The source has been observed mainly in its soft state, with short periods of flaring. We also observed low-frequency quasiperiodic oscillations. From a spectropolarimetric analysis, we associate a polarization to the accretion disk at $<3.2\%$ at 90% confidence level, compatible with expectations for an electron scattering dominated optically thick atmosphere at the Sco X-1 inclination of $\sim 44^\circ$; for the higher-energy Comptonized component, we obtain a polarization of $1.3\% \pm 0.4\%$, in agreement with expectations for a slab of Thomson optical depth of ~ 7 and an electron temperature of ~ 3 keV. A polarization rotation with respect to previous observations by OSO-8 and PolarLight, and also with respect to the radio-jet position angle, is observed. This result may indicate a variation of the polarization with the source state that can be related to relativistic precession or a change in the corona geometry with the accretion flow.

Unified Astronomy Thesaurus concepts: Polarimetry (1278); Spectropolarimetry (1973); Neutron stars (1108); Accretion (14); Stellar accretion disks (1579); Low-mass x-ray binary stars (939); X-ray telescopes (1825)

1. Introduction

Accreting weakly magnetized neutron stars (NSs) in low-mass X-ray binaries (LMXBs) accrete matter via Roche lobe overflow from a stellar companion of mass smaller than 1 $M_\odot$ (Bahramian & Degenaar 2023). The result of the matter overflowing the Roche lobe is the formation of an accretion disk around the compact object. Contrary to the case of black holes (BHs), the accreting gas interacts with the NS surface, forming a boundary layer (BL) coplanar to the disk (Shakura & Sunyaev 1988; Popham & Sunyaev 2001). However, the gas is not stopped immediately but spreads along the NS surface to high latitudes, forming a spreading layer (SL; Inogamov & Sunyaev 1999; Suleimanov & Poutanen 2006).

NS-LMXBs are very bright X-ray sources, and by studying their timing properties in the 1–10 keV band and/or their tracks in the X-ray hard-color/soft-color diagram (CCD) or hard-color/intensity diagram, they can be classified as Z- and atoll sources (Hasinger & van der Klis 1989; van der Klis 1989). The luminosity of Z-sources is higher ($\gtrsim 10^{37}$ erg s^{-1}, near or just below the Eddington luminosity) than that of the atoll sources (10^{36}–10^{37} erg s^{-1}), and they show a Z-like track in the CCD. Along such a track, three different branches can be clearly distinguished: horizontal (HB), normal (NB), and flaring (FB). They are correlated with the mass accretion rate, and not all of these branches are well distinguished in every Z-source (Schulz & Wijers 1993; Kuulkers et al. 1994). In addition, we can also identify a hard apex that separates the HB and the NB, and a soft apex (SA) that separates the NB and the FB (Church et al. 2012; Motta & Fender 2019). Z-sources can also be classified as Cyg-like and Sco-like sources (Kuulkers et al. 1994, 1997). Cyg X-2, GX 5−1, and GX 340+0 belong to the first group, while Sco X-1, GX 349+2, and GX 17+2 belong to the latter one. Cyg-like sources show the full Z-pattern with all the branches well visible; however, they have weak flaring compared to Sco-like sources. On the contrary, most of the latter ones show an HB that is hard to identify, and the flaring is more frequent and with a higher X-ray flux (Church et al. 2012). Moreover, Cyg-like sources may have a higher inclination (Kuulkers et al. 1997) or a higher magnetic field with respect to the Sco-like ones (Psaltis et al. 1995).

The X-ray spectrum of weakly magnetized NS-LMXBs can be typically described by two main components. The first is a blackbody or multicolor disk, which describes the softer thermal spectral emission from the accretion disk and/or the NS surface; the second is a harder Comptonization component, which describes the emission from electrons accelerated at the

[56] Deceased.

boundary between the accretion disk and the NS surface that occurs in the BL/SL region. In addition to these soft and hard components, an iron emission line at ∼6.4 keV can be observed in several weakly magnetized NSs as the prominent feature of reflection from the inner accretion disk. This is clear evidence of the presence of an external source of hard X-rays with respect to the colder disk, where the reflection process takes place. The iron line broadening is shaped by the gravitational redshift, the Doppler shift, and the relativistic Doppler boosting, giving a direct way to probe the physics of the region of strong gravity close to the compact object (see, e.g., Matt 2006; Cackett et al. 2008, 2010, 2012; Ludlam et al. 2018; Mondal et al. 2020, 2022; Ludlam et al. 2022). In particular, the reflection component allows one to determine the inner radius of the accretion disk and, applying suitable models, can provide estimates for the proximity of the illumination source to the disk through the emissivity profile and the reflection fraction (see, e.g., Wilkins 2018). The spectral and timing properties of these sources allow us to understand the basics of their emission mechanisms, but they are not able to fully constrain the geometry of the different emitting regions because the spectral features are degenerate from this point of view. At present, observations favor a scenario in which the BL/SL spectrum, represented to a certain accuracy by the Fourier frequency resolved spectrum, remains constant in the course of the luminosity variations (Gilfanov et al. 2003; Revnivtsev & Gilfanov 2006; Revnivtsev et al. 2013). This also means that quasiperiodic oscillations (QPOs) are associated with the harder spectral component, which is due to the contribution of BL/SL.

A tool to disentangle among possible emission geometries is X-ray polarization. In fact, different geometries of the corona can be associated with different X-ray polarization properties (as in the case of BH-LMXBs; Haardt & Matt 1993; Poutanen & Vilhu 1993; Poutanen & Svensson 1996; Schnittman & Krolik 2010), or by the accretion disk (Chandrasekhar 1960; Loskutov & Sobolev 1982), or by the BL/SL (Lapidus & Sunyaev 1985; Suleimanov & Poutanen 2006). Almost 40 yr after the first tentative attempts to measure X-ray polarization, the recent launch of the Imaging X-ray Polarimetry Explorer (IXPE; Soffitta et al. 2021; Weisskopf et al. 2022) adds X-ray polarization to spectral and timing information to investigate the geometry of the accretion flow in LMXBs. Aiming to obtain this, IXPE observed several weakly magnetized LMXBs: the two Z-sources Cyg X-2 (Farinelli et al. 2023) and GX 5−1 (Fabiani et al. 2023), the Z-atoll transient XTE J1701−462 (Cocchi et al. 2023; Jayasurya et al. 2023), the peculiar source Cir X-1 (Rankin et al. 2023), and three atoll sources: GS 1826−238 (Capitanio et al. 2023), GX 9+9 (Chatterjee et al. 2023; Ursini et al. 2023), and the ultracompact 4U 1820−303 (Di Marco et al. 2023a). The average 2–8 keV polarization is higher in the Z-sources than in the atoll ones, and it seems to vary with the position of the sources on the Z-track in the CCD (Cocchi et al. 2023; Fabiani et al. 2023; Rankin et al. 2023). For the Z-source Cyg X-2, IXPE measured a polarization angle (PA) that appears to be aligned with the radio jet (Farinelli et al. 2023).

Sco X-1 is a weakly magnetized NS-LMXB, and it is the brightest persistent and the first discovered extrasolar X-ray source (Giacconi et al. 1962). It has a peak luminosity near the Eddington limit; that is, for a 1.4 $M_\odot$ NS, $\sim 2 \times 10^{38}$ erg s^{-1} (Titarchuk et al. 2014). The companion is an M-type star of ∼0.4 $M_\odot$ (Steeghs & Casares 2002). The orbital period of the system estimated from optical observations is ∼19 hr (Gottlieb et al. 1975; Galloway et al. 2014). The distance to Sco X-1, $D = 2.13^{+0.21}_{-0.26}$ kpc, as derived in Gaia Data Release 2 (Arnason et al. 2021), is in agreement with the previous estimates obtained by parallax measured with the Very Long Baseline Array (Bradshaw et al. 1999). Sco X-1 was the first X-ray binary where radio emission was also detected (Andrew & Purton 1968). Very long baseline interferometry observations spatially resolved the jet at submilliarcsecond scales, revealing mildly relativistic motion of components in opposite directions at a position angle of ∼54° and inclination 44° ± 6° (Fomalont et al. 2001a, 2001b).

Being the brightest X-ray source in the sky, apart from the Sun, Sco X-1 was one of the first targets for X-ray polarization studies. In 1977, the OSO-8 satellite spent about 15 days observing it, obtaining a low-significance detection at 2.6 keV with a polarization degree (PD) of 0.4% ± 0.2% and PA of 29° ± 10°, and at 5.2 keV, PD = 1.3% ± 0.4% and PA = 57° ± 6° (Long et al. 1979). Recently, PolarLight observed Sco X-1 for a total of ∼322 days (Long et al. 2022), obtaining hints of variations of polarization with the energy and the source flux. In this case, a 5σ detection in the 4–8 keV energy band was obtained, but only when the flux was high: PD = 4.3% ± 0.8% and PA = 53° ± 5°. Although the polarization properties change with the emission state (Cocchi et al. 2023; Fabiani et al. 2023; Rankin et al. 2023), these measurements were performed in long exposures for which the emission state could not be determined, thus limiting the usefulness of these results.

2. X-Ray Observations

IXPE observed Sco X-1 on 2023 August 28 starting at 16:10 UTC (ObsID 02002401) for a total exposure of ≃24 ks per detector unit (DU). Because of the high X-ray flux from Sco X-1, the IXPE observations were performed using a partially opaque absorber, the so-called gray filter present in the detector's filter and calibration wheel (Ferrazzoli et al. 2020; Soffitta et al. 2021; Weisskopf et al. 2022). For such a bright source, this filter is needed to reduce the flux to a level compatible with the IXPE focal plane detector dead time. In particular, it allows for a tenfold reduction of the incident flux at low energies, below 3 keV. For the data analysis, we applied the most recent response matrices released in HEASOFT on 2023 June 16.

Jointly with IXPE, we planned strictly simultaneous observations with other facilities to have a better energy resolution and cover a broader energy band than those available with IXPE alone, aiming to obtain an accurate spectral model of the source simultaneous to the measurement of polarization. Our coordinated observations were (i) the Nuclear Spectroscopic Telescope Array (NuSTAR; ObsID 30902336002) from 2023 August 28 at 17:41 UTC to August 29 at 04:41 UTC; (ii) the Neutron Star Interior Composition Explorer (NICER; ObsIDs 6689010101 and 6689010102) on 2023 August 28 from 15:23 to 23:14 UTC and 2023 August 29 from 00:40 to 07:07 UTC, and (iii) the Hard X-ray Modulation Telescope (Insight-HXMT; ObsIDs P06053160010N, with N = 1–5) from 2023 August 28 at 15:30 to 19:11, from 2023 August 28 at 19:11 to 22:21, from 2023 August 28 at 22:21 to 2023 August 29 at 01:31, from 2023 August 29 at 1:31 to 4:42, and from 2023 August 29 at 4:42 to 7:27. The exposure times, after the dead-time correction, in each ObsID and for each

Table 1
Exposure Time in Each Observatory for Each Telescope/Instrument on Board and Observation ID

	ObsID	Telescope	Exp. Time (s)
IXPE	02002401	DU1	24456
		DU2	24456
		DU3	24456
NICER	6689020201		3039
	6689010102		2537
NuSTAR	30902036002	FPMA	932
		FPMB	1011
HXMT	P060531600101	ME	2093
		HE	3210
	P060531600102	ME	1236
		HE	1839
	P060531600103	ME	80
		HE	235
	P060531600104	ME	1324
		HE	687
	P060531600105	ME	1796
		HE	2460

instrument are reported in Table 1. For Insight-HXMT, the low-energy instrument is not well calibrated, and we excluded it from the analysis; the medium- (ME) and high-energy (HE) instruments were used in the analysis.

In Figure 1, we show the light curves of the source as observed with all the coordinated X-ray observatories. We note that all of them were strictly simultaneous with IXPE. We also observe flaring activity, causing a simultaneous increase in the count rate of the source for all the telescopes covering different energy bands.

To investigate the state of the source during the observations, we calculated the CCD considering all the observations of Sco X-1 in the NuSTAR data archive (ObsIDs 30001040002 and 30502010002). In Figure 2, we show the CCD obtained from the archival observations together with those performed during the IXPE run. We can conclude that during the IXPE observation, Sco X-1 is moving from the FB to the NB and then again to the FB of the Z-track. The two passages and the fact that the source never entered deeply into the NB produced an IXPE observation dominated by the SA, with short periods in the FB.

We detected a transient QPO in NICER ObsID 6689010102. Using the STINGRAY package (Huppenkothen et al. 2019), we produced a Bartlett (1948) periodogram (an estimate of the power density spectrum) of the full ObsID, averaging the periodograms calculated in 153 intervals of equal length (16 s each). We found a clear ∼6 Hz QPO, and we proceeded to verify whether its properties changed during the observation. We then inspected a dynamical power spectrum, showing the change of the QPO in subsets of the observation, and it was immediately clear that the QPO disappeared after the first good time interval (GTI) of the observation and reappeared in the last, with no major changes of amplitude or frequency inside a given GTI. We proceeded to analyze the periodograms on a per-GTI basis. This time, we chose a smaller segment size (8 s) to improve the statistics at the expense of some frequency resolution. We fit a model comprising a Poisson noise level, a QPO at ∼6 Hz, and an optional power law when required by the low-frequency data. We used the maximum-likelihood method, based on the Whittle statistics, described by Barret & Vaughan (2012) and implemented in the STINGRAY.MODELING subpackage. Since the analysis of the QPO is not the main focus of the paper, we quote the 1σ error bars from the fitting routine used internally by STINGRAY, knowing that the estimates might be slightly off. In the first GTI (31 s), the QPO had a central frequency of 7.2 ± 0.2 Hz peak and a FWHM of 3.0 ± 0.5 Hz (quality factor $\nu/\Delta\nu \approx 2.4$) at 68% confidence level (CL). In the last GTI (805 s), the peak was at 6.07 ± 0.01 Hz, and the FWHM was 2.27 ± 0.01 Hz ($\nu/\Delta\nu \approx 2.7$) at a 68% CL. Figure 3 shows the second QPO and the best-fit model. These frequencies are compatible with the CCD result; the source, in the beginning, was in a flaring state (QPO ∼ 7 Hz), then moved toward the NB (but never entered it), staying in the SA; just before the end of the observation, a short flaring state is observed, then the source came back to the SA, where a 6–7 Hz range for QPOs is expected as reported by, e.g., Casella et al. (2006).

3. Polarimetric Analysis

We estimated the X-ray polarization by using IXPEOBSSIM software (Baldini et al. 2022) with the `PCUBE` algorithm based on the Kislat et al. (2015) method, which allows for a model-independent analysis of the polarization.

As reported in the IXPEOBSSIM notes[57] and Veledina et al. (2023), the polarization obtained by the `PCUBE` algorithm, when using the gray filter, does not properly account for the telescope response matrices at low energy. In particular, an overestimate of the polarization below 3 keV is observed with respect to the one obtained by the more solid XSPEC (Arnaud 1996) spectropolarimetric analysis, which properly considers the response matrices of the instrument at low energy. The spectropolarimetric analysis is reported in detail in Section 5. Therefore, we decided to use the `PCUBE` algorithm only in the 3–8 keV band. We analyzed the IXPE data, following the prescription reported in Di Marco et al. (2023b). For bright sources, the background region is dominated by the source counting rate itself, that is, any way, at least one order of magnitude lower than the source signal on the whole IXPE energy band. Therefore, no background rejection is needed, and no background subtraction has to be performed. We analyzed the polarization as a function of the energy with bins of 1 keV; the results are shown in Figure 4(a) and reported in Table 2. The Stokes parameters show no evidence of a PD variation with energy or any rotation of the PA, as can also be seen in the polar plot for the X-ray polarization of Figure 4(b), where the contours at 68% CL for all the energy bins are well compatible. Thus, we can combine all the energy bins to derive the polarization in the 3–8 keV energy band, as reported in both Figure 4(c) and Table 2. The resulting polarization is PD $= 1.08\% \pm 0.15\%$ and PA $= 10^\circ \pm 4^\circ$ at 68% CL. The probability of obtaining such polarization in the case of an unpolarized source is 6×10^{-12}, corresponding to a detection significant at $\sim 7\sigma$ CL.

We also tried to separate the flaring activity of the source from the nonflaring state. The two different time intervals are defined by the shaded regions reported in Figure 1. The polarimetric results are reported in Figure 5, which shows that the confidence regions for the two intervals are compatible within 90% CL, although it seems to present a marginal

[57] https://github.com/lucabaldini/ixpeobssim/issues/714

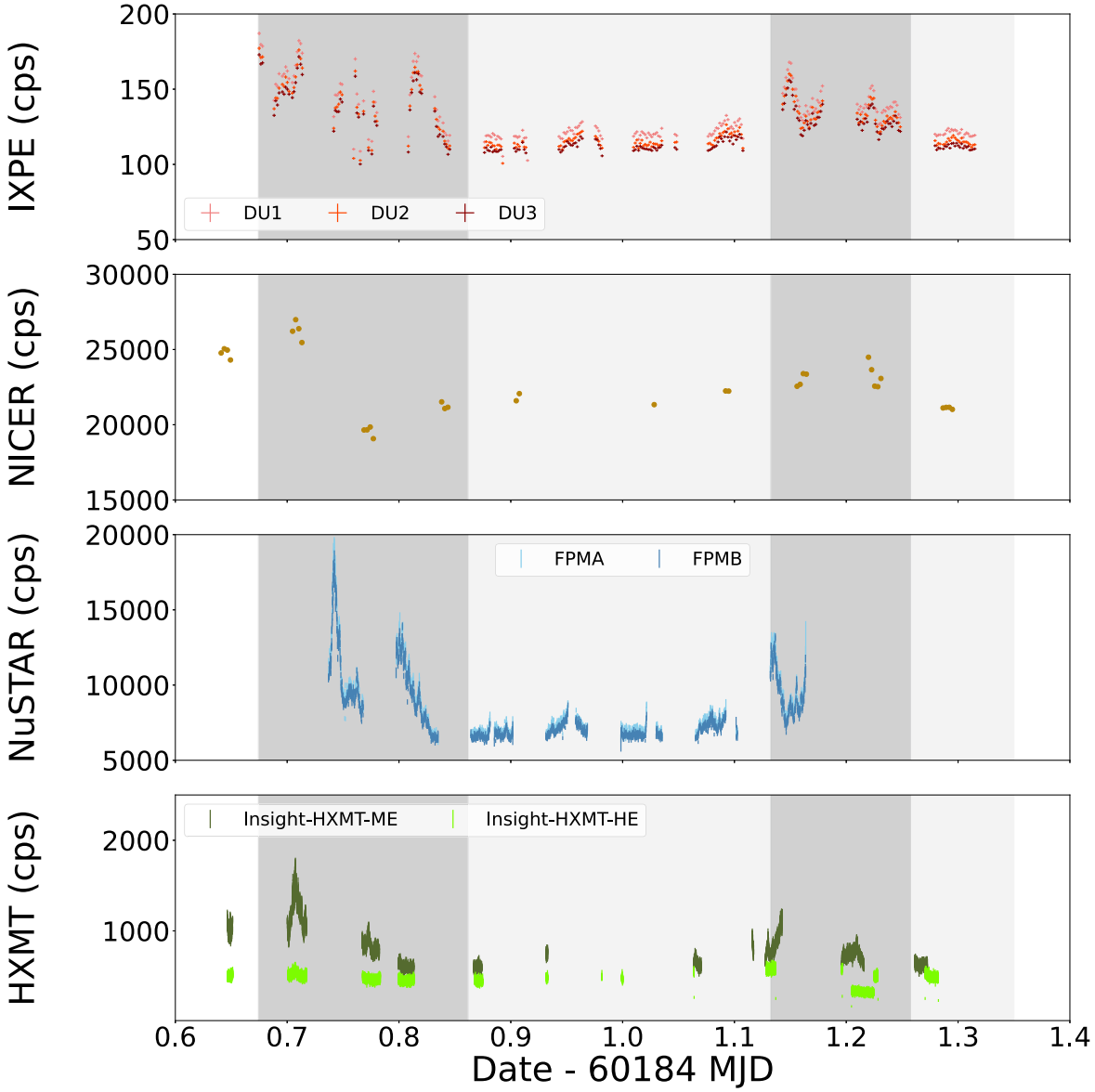

Figure 1. Light curves from the simultaneous observations of Sco X-1, from top to bottom: IXPE (DU1, DU2, and DU3), NICER, NuSTAR (FPMA and FPMB), and Insight-HXMT. They show that all the observations are well overlapped with the IXPE one. The flaring activity of the source is seen in all the simultaneous observations (dark gray shaded regions), while the nonflaring periods are identified with the light gray bands.

indication for a slightly higher PD in the flaring state. Therefore, considering that the present data do not allow for clearly observing a PD variation in the two states and, as reported in Mazzola et al. (2021), that no strong spectral variation in the different Sco X-1 states is reported, the analysis that follows will be carried out without dividing into flaring and nonflaring states.

4. Spectral Analysis

Here, we performed spectral modeling for the coordinated observations using the data from (i) NICER in 1.5–12 keV (we ignored data below 1.5 keV that can be affected by the daytime light loading reported in 2023 May), (ii) NuSTAR in 3–40 keV, (iii) the Insight-HXMT ME (in 8–30 keV, ignoring the 20–23 keV energy band to avoid effects related to the presence of Ag in the Si-pin detectors; Li et al. 2020) and HE (in 30–40 keV) telescopes, and (iv) IXPE in 2–8 keV unweighted spectra (Di Marco et al. 2022a). In NuSTAR and Insight-HXMT HE, events above 40 keV are excluded in the analysis because the spectrum is dominated by background; see the Appendix for details about data extraction. On the basis of the spectral models reported in the literature (Mazzola et al. 2021; Ding et al. 2023), we applied the simple model `tbabs*(diskbb+nthcomp)` in XSPEC v.12.13.0c (Arnaud 1996) to describe the continuum. We also used energy-independent cross-normalization factors between the different X-ray observatories and telescopes. To estimate the absorption from the interstellar medium, we set the abundances at the `wilm` values (Wilms et al. 2000) and froze $N_{\rm H}$ at the galactic value of 0.15×10^{22} cm^{-2} (Dickey & Lockman 1990; Kalberla et al. 2005; HI4PI Collaboration et al. 2016). About `nthcomp` (Zdziarski et al. 1996; Życki et al. 1999), we froze the `inp_type` to 0, corresponding to blackbody seed photons emitted from, e.g., the NS SL/BL. The resulting fit for this model is reported in Table 3. We also estimated the optical depth τ of the

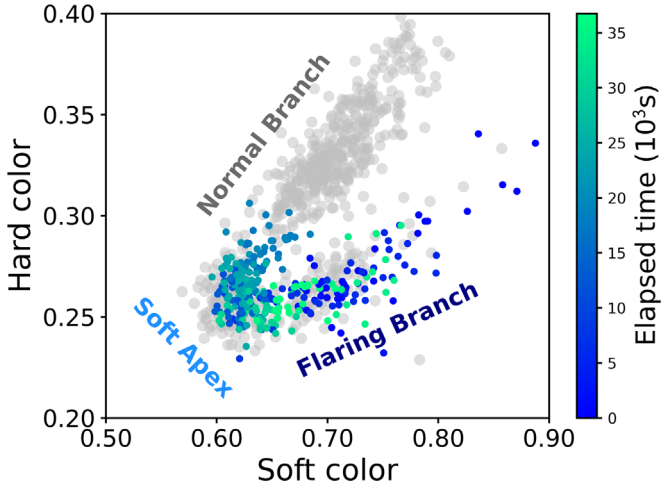

Figure 2. Color–color diagram from the NuSTAR data. The soft color is defined as the source count rate in the 6–10 keV band divided by the one in 3–6 keV, while the hard color is the ratio of the 10–20 keV count rate to the one in 6–10 keV. Gray points represent the past NuSTAR observations, while the colored ones report from blue to green the elapsed time since the start of the present NuSTAR observation simultaneous with IXPE.

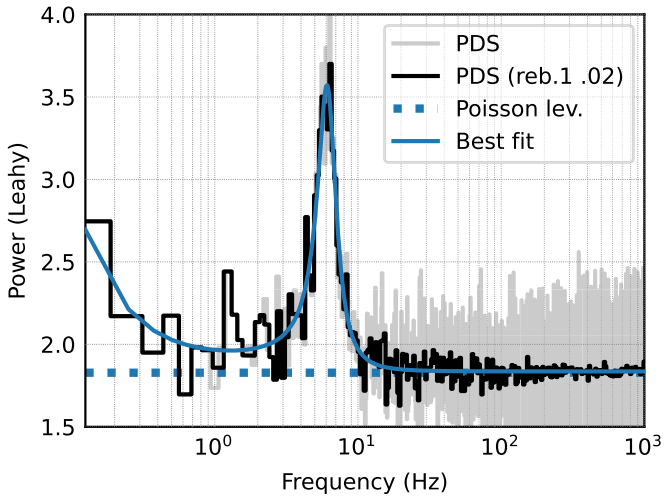

Figure 3. Bartlett (1948)–like periodogram from the last 805 s of NICER ObsID 6689010102, obtained by averaging 100 periodograms from 8 s segments of the light curve, normalized as in Leahy et al. (1983) in gray and rebinned geometrically (factor 1.02) to improve the signal-to-noise ratio at high frequencies (black). In blue, we plot the best-fit model consisting of a Poisson noise level, significantly below 2 due to dead time; a power-law red-noise component at low frequencies; and a QPO.

Comptonization component from the asymptotic power-law photon index Γ of `nthcomp`, using the relation

$$\Gamma = \left[\frac{9}{4} + \frac{1}{\tau\left(1+\frac{\tau}{3}\right)\frac{kT_e}{m_e c^2}}\right]^{1/2} - \frac{1}{2},$$

reported in Zdziarski et al. (1996). The obtained values for the optical depth are reported in the same table. The continuum spectrum fit shows a bad χ^2/dof (5365/2890 = 1.9) and a clear excess at ∼6.7 keV due to the presence of an iron fluorescence line. This residual excess is shown in Figure 6. Due to the worst spectral capabilities, this is not well visible in the IXPE data but is evident in the NuSTAR and NICER ones. Hereafter, no model-dependent systematic was applied to the fits, and, when not

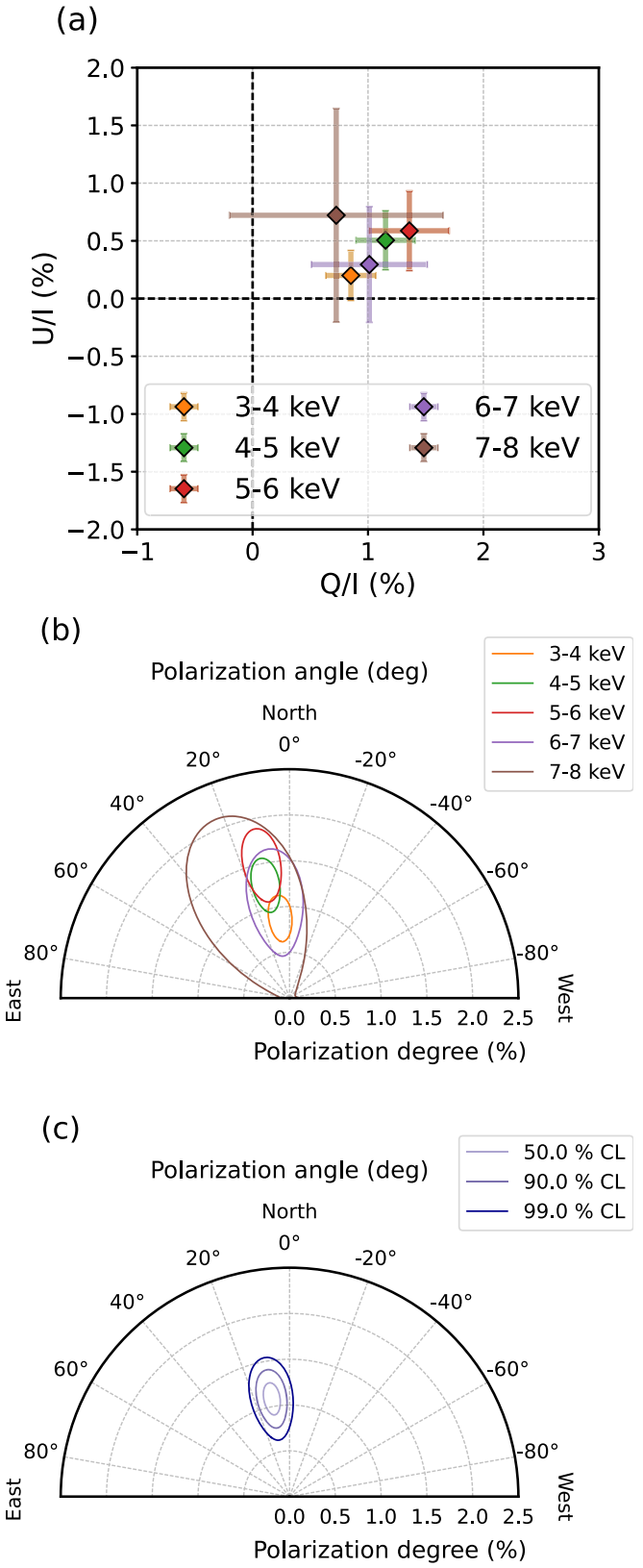

Figure 4. In these plots, the Sco X-1 polarization in different energy bins, as measured with `PCUBE` in `IXPEOBSSIM`, is reported. (a) Normalized Stokes parameters plane in 1 keV energy bins: Q/I vs. U/I. (b) Polar plot of the X-ray polarization when 1 keV binning is applied; contours are given at 68% CL. No trend of polarization varying with energy is visible in either (a) or (b). (c) Polar plot of the X-ray polarization in the 3–8 keV energy band; contours correspond to 50%, 95%, and 99% CL. The detection significance of the energy averaged polarization is at ∼7σ CL.

Table 2
Polarization Properties of Sco X-1 Obtained with the PCUBE Algorithm and the Spectropolarimetric XSPEC Analysis, Applied to Model A of Table 3

	PCUBE				XSPEC			
Energy Bin (keV)	PD (%)	PA (deg)	Q/I (%)	U/I (%)	PD (%)	PA (deg)	Q/I (%)	U/I (%)
2–3	⋯	⋯	⋯	⋯	0.9 ± 0.3		-4 ± 10	0.9 ± 0.3
-0.1 ± 0.3								
3–4	0.9 ± 0.2	7 ± 7	0.9 ± 0.2	0.2 ± 0.2	0.9 ± 0.2	7 ± 7	0.9 ± 0.2	0.2 ± 0.2
4–5	1.3 ± 0.3	12 ± 6	1.2 ± 0.3	0.5 ± 0.3	1.2 ± 0.3	12 ± 6	1.1 ± 0.3	0.5 ± 0.3
5–6	1.5 ± 0.3	12 ± 7	1.4 ± 0.3	0.6 ± 0.3	1.5 ± 0.3	12 ± 7	1.3 ± 0.3	0.6 ± 0.3
6–7	1.1 ± 0.5	8 ± 13	1.0 ± 0.5	0.3 ± 0.5	1.1 ± 0.5	5 ± 13	1.1 ± 0.5	0.2 ± 0.5
7–8	$1.0^{+0.9}_{-0.7}$	22 ± 26	0.7 ± 0.9	0.7 ± 0.9	$0.7^{+0.9}_{-0.7}$	14 ± 14	0.6 ± 0.9	0.3 ± 0.9
3–8	1.08 ± 0.15	10 ± 4	1.02 ± 0.15	0.38 ± 0.15	1.08 ± 0.15	10 ± 4	1.01 ± 0.14	0.37 ± 0.14
4–8	1.25 ± 0.20	12 ± 5	1.11 ± 0.20	0.51 ± 0.20	1.25 ± 0.18	11 ± 4	1.16 ± 0.18	0.48 ± 0.18

Note. Errors are reported at 68% CL.

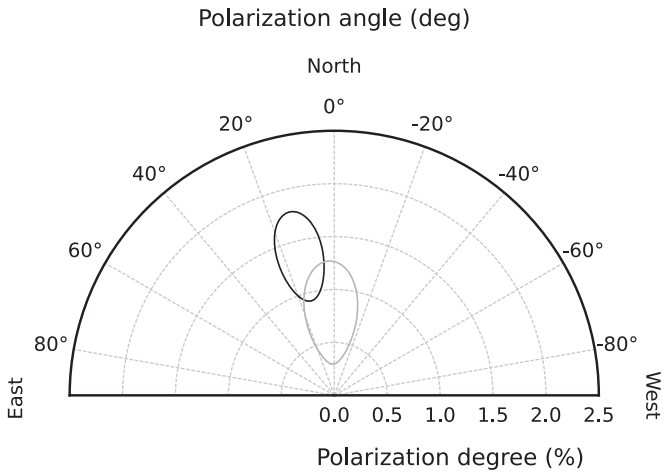

Figure 5. Polar plot of the X-ray polarization for Sco X-1 in the two different flaring (dark gray) and nonflaring (light gray) states; the two states show a compatible polarization. The contours are at 90% CL.

explicitly reported, the uncertainties are always at 90% CL. To take into account NuSTAR calibration uncertainties (Grefenstette et al. 2022; Madsen et al. 2022), we allow the offset in the gain to vary by the quoted ∼40 eV systematic uncertainty and find a best fit of ∼80 eV for focal plane modules A and B (FPMA and FPMB); similarly, for IXPE calibration uncertainties (Di Marco et al. 2022b; Rankin et al. 2023), we left free the gain slope and offset, obtaining a slope of $\sim 0.94\,\mathrm{keV}^{-1}$ and an offset of ∼70 eV. Also, for Insight-HXMT ME, we applied these gain corrections, obtaining $1.033 \pm 0.001\,\mathrm{keV}^{-1}$ for the slope and an offset of -0.205 ± 0.014 keV. No strong variations in the different adopted models of Table 3 are present; thus, these values are representative of all of them.

Aiming to describe the Fe line component, we tried to fit the spectrum with model A of Table 3, which includes a broad Gaussian line, as in Di Marco et al. (2023b). The resulting fit shows a strong improvement of the χ^2/dof ($3033/2887 = 1.05$) with reduction by a factor of ∼1.8. The spectral fit for this model is shown in Figure 7.

Aiming to model this Fe line better, instead of a Gaussian, we tested a `diskline` component (Fabian et al. 1989) in model B: `tbabs*(diskbb+nthcomp+diskline)`. As reported in Table 3, the resulting χ^2/dof is 3083/2886, with no improvement with respect to the Gaussian in terms of reduced χ^2, but we obtain for the inner disk a radius of 11 ± 4, R_g 90% CL, which corresponds to $1.83R_{\mathrm{ISCO}}$, meaning that the disk during the observation is near the NS surface.

We have also attempted to fit with a complete reflection model, `relxillNS` in the XILLVER code (García et al. 2022), reported as model C in Table 3: `tbabs*(diskbb+nthcomp+relxillNS)`. In this model, we assumed most of the X-ray continuum emission as thermal, originating from either the surface of the NS or the SL/BL and described by a blackbody with the same temperature as the seed photons in `nthcomp`. Then, it illuminates the accretion disk, producing the reprocessed/reflected X-ray spectrum of the reflection component. `xillverNS` (García et al. 2022) solves this radiation transfer problem in a plane-parallel slab, providing an angle-dependent spectrum emergent at the top of this slab for a given irradiation, gas density, and elemental abundances. `relxillNS` used in this analysis represents a complete relativistic model taking into account the angular distribution of the solution provided by `xillverNS` and correctly predicts the integrated reflection of the disk by including all relativistic effects (such as distortion of the spectral features due to relativistic corrections such as boosting, gravitational redshift, and Doppler effects). In this model, we froze the density $\log N$ parameter to 19, that is, the maximum value for which the model is calculated (García et al. 2022); the outer radius to $1000R_g$, as in model B; and the reflection fraction to −1 to obtain only the spectral component due to the reflected fraction, and the NS spin is fixed to 0 ($R_{\mathrm{ISCO}} = 6R_g$). The iron abundance, when it is left free to vary, tends to be as high as possible; thus, we fixed it to an acceptable value equal to 4, allowing us to still obtain a good reduced χ^2 (this situation is similar to the case of Cyg X-1, where high iron abundance was inferred; Tomsick et al. 2018). When left free to vary, the inclination becomes $79° \pm 30°$ at 68% CL, and it is unconstrained at 90% CL. This value is compatible, given the large uncertainty, with the more accurate one from Fomalont et al. (2001a, 2001b); for this reason, we froze it in the final analysis to the literature value of 44°.

When this model is applied, we obtain an improvement in terms of reduced χ^2 and F-test (probability 7×10^{-12}) with respect to model A. From this fit, we obtain an upper limit on the inner disk truncation radius of $9R_g$, which corresponds to $1.50R_{\mathrm{ISCO}}$. This result is compatible with the one obtained by the `diskline` modeling, confirming the presence of a disk

Table 3
Best-fit Parameters of the Spectral Models Applied to the Simultaneous Data from NICER, NuSTAR, Insight-HXMT, and IXPE

Component	Parameter (units)	Continuum	Model A	Model B	Model C
tbabs	$N_{\rm H}$ (10^{22} cm^{-2})	0.15	0.15	0.15	0.15
diskbb	$kT_{\rm in}$ (keV)	0.692 ± 0.004	0.683 ± 0.011	0.694 ± 0.01	0.87 ± 0.02
	norm ($[R_{\rm in}/D_{10}]^2 \cos\theta$)	25500 ± 700	25500 ± 1400	24300 ± 1200	10800 ± 800
	$R_{\rm in}$[a] (km)	40.1 ± 1.1	40.1 ± 2	39 ± 2	26 ± 2
nthcomp	Γ	2.78 ± 0.02	2.58 ± 0.02	2.61 ± 0.03	2.59 ± 0.03
	τ	5.95 ± 0.04	6.70 ± 0.05	6.62 ± 0.08	6.71 ± 0.08
	$kT_{\rm e}$ (keV)	3.41 ± 0.03	3.21 ± 0.03	3.23 ± 0.03	3.22 ± 0.04
	$kT_{\rm bb}$ (keV)	1.148 ± 0.008	1.08 ± 0.01	1.10 ± 0.01	1.24 ± 0.02
	norm	6.34 ± 0.05	6.94 ± 0.16	6.74 ± 0.17	4.19 ± 0.17
gauss	$E_{\rm line}$ (keV)	⋯	6.72 ± 0.02	⋯	⋯
	σ (keV)	⋯	0.45 ± 0.03	⋯	⋯
	norm (photon cm^{-2} s^{-1})	⋯	0.14 ± 0.01	⋯	⋯
	Equivalent width (eV)	⋯	66.836 ± 0.014	⋯	⋯
diskline	$E_{\rm line}$ (keV)	⋯	⋯	6.70 ± 0.02	⋯
	Emissivity	⋯	⋯	2.13 ± 0.09	⋯
	$R_{\rm in}$ (GM/c^2)	⋯	⋯	11 ± 4	⋯
	$R_{\rm out}$ (GM/c^2)	⋯	⋯	1000[b]	⋯
	Inclination (deg)	⋯	⋯	44[b]	⋯
	norm (photon cm^{-2} s^{-1})	⋯	⋯	$0.130^{+0.007}_{-0.003}$	⋯
	Equivalent width (eV)	⋯	⋯	65.38 ± 0.01	⋯
relxillNS	Emissivity	⋯	⋯	⋯	1.9 ± 0.1
	$R_{\rm in}$ (GM/c^2)	⋯	⋯	⋯	<9
	$R_{\rm out}$ (GM/c^2)	⋯	⋯	⋯	1000[b]
	Inclination (deg)	⋯	⋯	⋯	44[b]
	$\log\xi$	⋯	⋯	⋯	$2.48^{+0.04}_{-0.03}$
	$A_{\rm Fe}$	⋯	⋯	⋯	4[b]
	$\log N$	⋯	⋯	⋯	19[b]
	norm	⋯	⋯	⋯	0.078 ± 0.004
	χ^2/dof	5365/2890 = 1.9	3033/2887 = 1.05	3083/2886 = 1.06	2988/2886 = 1.03
		Cross-normalization factors			
	$C_{\rm NICER}$	1.0	1.0	1.0	1.0
	$C_{\rm NuSTAR-A}$	1.226 ± 0.002	1.226 ± 0.002	1.226 ± 0.002	1.225 ± 0.002
	$C_{\rm NuSTAR-B}$	1.190 ± 0.002	1.190 ± 0.002	1.190 ± 0.002	1.190 ± 0.002
	$C_{\rm HXMT-ME}$	1.144 ± 0.003	1.1462 ± 0.003	1.1463 ± 0.003	1.148 ± 0.003
	$C_{\rm HXMT-HE}$	1.3 ± 0.2	1.4 ± 0.2	1.4 ± 0.2	1.4 ± 0.2
	$C_{\rm IXPE-DU1}$	1.090 ± 0.002	1.089 ± 0.002	1.089 ± 0.002	1.088 ± 0.002
	$C_{\rm IXPE-DU2}$	1.062 ± 0.002	1.061 ± 0.002	1.061 ± 0.002	1.061 ± 0.002
	$C_{\rm IXPE-DU3}$	1.004 ± 0.002	1.003 ± 0.002	1.003 ± 0.002	1.003 ± 0.002
		Photon flux ratios in 2–8 keV			
	$F_{\rm diskbb}/F_{\rm tot}$	0.23	0.21	0.22	0.32
	$F_{\rm nthcomp}/F_{\rm tot}$	0.77	0.78	0.77	0.59
	$F_{\rm gauss,diskline,relxillNS}/F_{\rm tot}$	⋯	0.01	0.01	0.09

Notes. The NICER flux in 2–8 keV is 1.98×10^{-7} erg s^{-1} cm^{-2}, corresponding to the luminosity of 1.02×10^{38} erg s^{-1} ($\sim$0.6 $L_{\rm Edd}$ for a 1.4 $M_\odot$ NS). Errors are reported at 90% CL.

[a] The inner radius for the diskbb component is estimated assuming an inclination at 44°, as reported in Fomalont et al. (2001a), and a distance of 2.13 kpc (Arnason et al. 2021).

[b] Fixed.

close to the NS surface. This model, when applied, shows a relative flux for the reflection component at a level of 10%, which is a minor contribution with respect to the disk (26% in this model) and the Comptonization, which is dominating in all the applied spectral models (>64%).

The obtained results for the spectral model are consistent with the previous one reported by Mazzola et al. (2021) for the continuum, while they do not apply a full reflection modeling, giving no result for the inner radius from this latter one. Therefore, in this paper, we obtained a measurement of the inner radius for Sco X-1 from the reflection modeling for the first time. This result is consistent with the one obtained for the Sco-like Z-source GX 349+2 by Coughenour et al. (2018), where an inner radius at the $R_{\rm ISCO}$ level is found in the SA and FB states (except the extreme flaring one). A similar result was also obtained by Ludlam et al. (2022) for Cyg X-2.

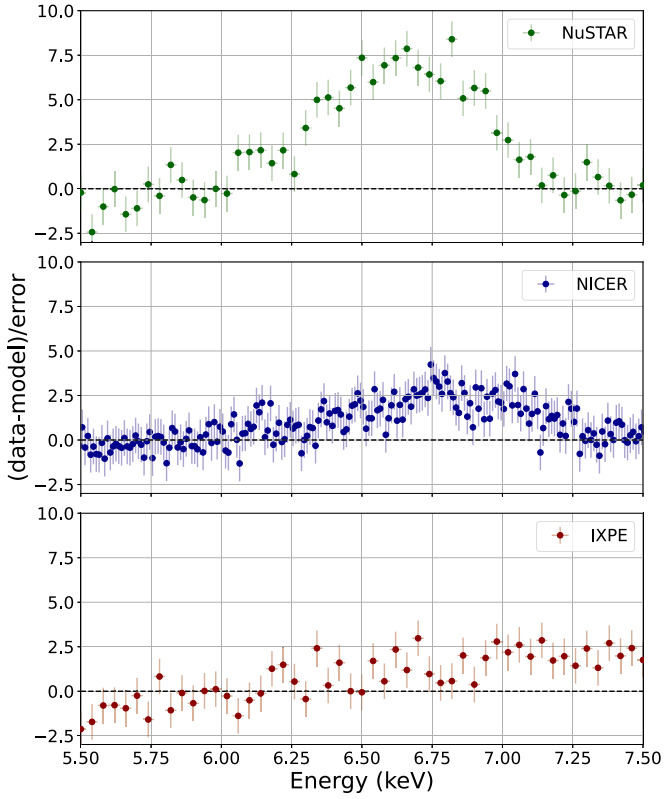

Figure 6. Spectral residuals in the energy range 5.5–7.5 keV for the Sco X-1 observations with NuSTAR-FPMA (top), NICER (center), and IXPE-DU1 (bottom), when the spectral model which represents the continuum, without any component describing the Fe line complex. The NuSTAR and NICER data show an excess compatible with a broad iron line, indistinguishable in the IXPE spectrum due to its limited spectral capabilities.

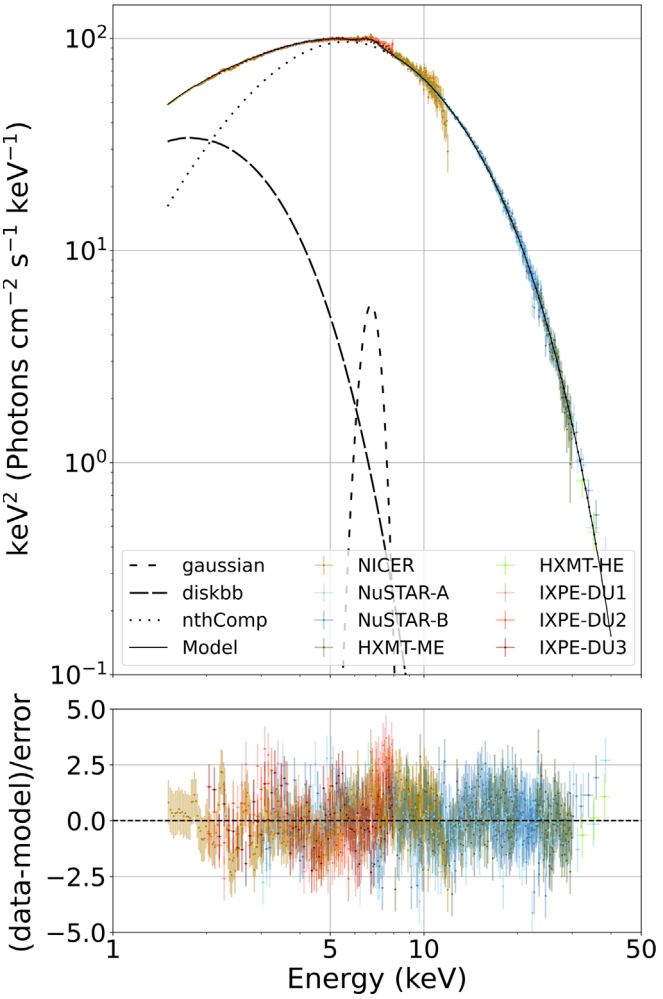

Figure 7. Spectral energy distribution of Sco X-1 in EF_E representation. The points show the data from NICER (brown), NuSTAR (blue), Insight-HXMT (green), and IXPE (red). The different spectral model components are reported with black lines for `diskbb` (long-dashed), `nthcomp` (dotted), and `gauss` (short-dashed). The bottom panel shows the residuals between the data and the best-fit model A.

5. Spectropolarimetric Analysis

We analyzed the polarimetric data by using XSPEC v.12.13.0c (Arnaud 1996), first freezing the spectral model at the simplest model A reported in Section 4 with the best-fit values reported in Table 3. The spectral features due to the reflection, including the broad Fe line, are hardly distinguishable with the IXPE energy resolution and narrow energy band. When model A is applied only to the IXPE I spectra, we get a $\chi^2/\mathrm{dof} = 497/436 = 1.14$. Therefore, we fitted I, Q, and U spectra simultaneously (applying the same gain corrections to their responses) using the simple model `tbabs*polconst*(diskbb+nthcomp+gauss)` to compare the spectropolarimetric results with the one obtained by `PCUBE`. The polarization in the IXPE nominal 2–8 keV energy band is PD $= 1.0\% \pm 0.2\%$ and PA $= 8° \pm 6°$ at 90% CL with a $\chi^2/\mathrm{dof} = 1333/1337 = 1.00$. When this analysis is applied in the same 3–8 keV energy band of `PCUBE`, as reported also in Table 2, the polarization values are well compatible within 68% CL. The same results are obtained when the IXPE nominal energy band is divided into 1 keV energy bins (see Table 2). This spectropolarimetric analysis also allows us to determine the polarization values in the 2–3 keV energy bin, where the `PCUBE` algorithm overestimates the polarization. The PD and PA values in 2–3 keV are compatible with the ones at higher energies within 68% CL, confirming no significant variations of polarization with energy.

As the iron line emission is not expected to be polarized because of their isotropic emission (see, e.g., Churazov et al. 2002), we fitted the data with a more physical model, `tbabs*(polconst*(diskbb+nthcomp)+gauss)`, with an unpolarized Gaussian line. The result is compatible with the one of the previous model, obtaining in the 2–8 keV energy band PD $= 1.0\% \pm 0.2\%$ and PA $= 8° \pm 6°$ at 90% CL with a $\chi^2/\mathrm{dof} = 1371/1341 = 1.02$. For this model, we also tried to apply a polarization varying linearly with energy by using the `pollin` model instead of `polconst`; the result is a slope compatible with zero for both PD and PA ($A_{\mathrm{slope}} = (0.11 \pm 0.18)\%\ \mathrm{keV}^{-1}$, $\psi_{\mathrm{slope}} = (3° \pm 5°)\ \mathrm{keV}^{-1}$ at 90% CL), as expected from the results in the `PCUBE` analysis; see Table 2. In conclusion, model-dependent spectropolarimetric analysis confirms no evidence of variation of PD or PA in the IXPE nominal energy band.

To complete our spectropolarimetric analysis, we applied a different model with `polconst` associated at each spectral component, considering an unpolarized Gaussian line: `tbabs*(polconst*diskbb+polconst*nthcomp+gauss)`. This model can allow us to disentangle polarization of the disk emission from the one due to Comptonization in the SL/BL. The results for this fit are reported in Table 4 and Figure 8. For the disk component, we obtained a PD of $1.5\% \pm 1.0\%$ and a PA of $-40° \pm 21°$ at 68% CL, corresponding to an upper limit for the PD of $<3.2\%$ at 90% CL.

Table 4
Best-fit Parameters for the Spectropolarimetric Analysis with the Model `polconst*diskbb+polconst*nthcomp+gauss`

Component		Value
`diskbb`	PD (%)	<3.2
	PA (deg)	...
`nthcomp`	PD (%)	1.3 ± 0.4
	PA (deg)	14 ± 8
	χ^2/dof	$1329/1337 = 0.99$

Note. Errors are at 90% CL.

For the Comptonization component, we obtained a PD of $1.3\% \pm 0.4\%$ and a PA of $14^\circ \pm 8^\circ$ at 90% CL.

As a further step, we tried to apply the spectropolarimetric analysis to model C, including modeling for the reflection component, aiming to better understand its contribution to the total polarization. First, we associate a different constant polarization to each spectral component, but, due to the limited spectral capabilities of IXPE, a clear polarimetric disentanglement of the three components in the Q and U spectra is not possible. As a result, just upper limits at 90% CL of <1.9% for the disk component, <8.2% for the Comptonized component, and <66% for the reflection one can be obtained. Then, we fixed the PD and PA for the disk and Comptonization components to the values of Table 4, obtaining a PD of the reflection of <6.4%, still unconstrained at 90% CL. As a latter scenario, we tried to fix the PD of the diskbb at 1.1%, corresponding to the classical results of Chandrasekhar (1960) for an inclination of 44°, with PA at −40°, and we assumed an unpolarized Comptonization component. In this case, we obtained PD = $14\% \pm 5\%$ and PA = $15^\circ \pm 7^\circ$ (errors at 90% CL) for the reflection.

6. Discussion

IXPE observed Sco X-1 mainly in the SA state with short periods in the FB, as shown by the NuSTAR CCD of Figure 2 and also by the presence of QPOs in NICER data (see Figure 3). As shown in Figure 5, no evidence for variation of polarization between these two states is observed. The average polarization, representative of the SA state, is measured to be PD = $1.1\% \pm 0.2\%$ and PA = $10^\circ \pm 7^\circ$ in the 3–8 keV energy band by the model-independent `PCUBE` analysis (significance $\sim 7\sigma$ CL). The XSPEC spectropolarimetric analysis in the whole IXPE 2–8 keV nominal energy band applied to the simple model A of Table 3, assuming an unpolarized Gaussian, results in an average PD of $1.0\% \pm 0.2\%$ and a PA of $8^\circ \pm 6^\circ$ (errors at 90% CL).

An energy-resolved analysis applying a 1 keV binning has been performed, and no significant evidence for variation with energy of the PD or PA is observed in either the `PCUBE` analysis or the XSPEC one. Also, an attempt to fit the data with the `pollin` XSPEC model confirms PD and PA to be constant in the whole IXPE nominal 2–8 keV energy band. This result is different, e.g., from the previous one obtained by IXPE for the ultracompact 4U 1820–303 (Di Marco et al. 2023a). The observed constant polarization, even if smaller than expectations, can be compatible with a corona geometry, as in the case C of Poutanen et al. (2023) proposed for a BH in the hard state, where the hot medium is situated within the truncated cold accretion disk with the seed unpolarized photons coming from the outer cold truncated disk having incident angles limited by the aspect ratio of the flow. Although this geometry is not compatible with the present observation, where Sco X-1 is in a soft state and the disk approaches the NS surface, the most important aspect of the model is the angular distribution of the incident seed photons for scattering. Thus, this model can give some indication of a geometry for which no variation of PD/PA with energy is expected. Alternative scenarios are discussed in Schnittman & Krolik (2010), where such behavior is expected for a sandwich corona in active galactic nuclei, and in Gnarini et al. (2022) for a sandwich/wedge and/or a shell corona.

When a different polarization is associated with each spectral component of model A, we obtain an upper limit of <3.2% at 90% CL for the PD of the disk component, compatible with expectations for an electron scattering–dominated, optically thick accretion disk (Chandrasekhar 1960; Sobolev 1963) that is ∼1.1% for an inclination of ∼44° as measured for Sco X-1 (Fomalont et al. 2001a). For the Comptonized component, we measured a PD of $1.3\% \pm 0.4\%$, compatible with the result obtained for a Thomson optical depth $\tau_T \sim 7$ and $kT_e \sim 3$ keV (see Figure 5 in Sunyaev & Titarchuk 1985).

Sco X-1 spectral analysis of the multiobservatory observations also allows for the study of the reflection component. In Coughenour et al. (2018), a study of the reflection in the Sco-like source GX 349+2 showed a strong agreement between different states along the Z-track; except for the extreme FB, this agrees with the good reduced χ^2 we obtain mixing the SA state and the short flaring states in the present observations. For GX 349+2, they reported an average inner radius of about 33 km that is not varying in the different states, except the extreme flaring; this R_{in} value is larger with respect to the present estimate obtained for Sco X-1, which is ∼18 km for a canonical 1.4 $M_\odot$ NS. This means that in the present Sco X-1 observation, the average inner radius is closer to the NS surface, which can be considered an upper limit on the NS radius. An alternative estimate of the inner disk radius can also be obtained by the `diskbb` component used to describe the continuum in the different models of Table 3; in model C, when from the `diskbb` result for nonzero-torque boundary condition we obtain a slightly larger R_{in}, at level of $13R_g$, but still confirming a disk approaching the NS surface.

The XSPEC spectropolarimetric analysis has also been applied to model C, which includes modeling of the reflection component. To achieve a constrained polarization estimate for the reflection component, we need to fix the PD for the disk at 1.1% (corresponding to the classical results of Chandrasekhar 1960 for $i = 44^\circ$) with PA = −40° and assume an unpolarized Comptonization component that is almost the case reported in Figure 5 of Sunyaev & Titarchuk (1985) for an optical thickness of ∼7 (see Table 3). In this scenario, we obtain PD = $14\% \pm 5\%$ and PA = $15^\circ \pm 7^\circ$ (errors at 90% CL), compatible with the predicted polarization values for a Compton-reflected spectrum from cold matter, as reported by Matt (1993) and Poutanen et al. (1996).

Sco X-1 is a bright radio source, where radio jets were clearly identified (Andrew & Purton 1968; Bradshaw et al. 1999; Fomalont et al. 2001a). These radio jets are connected to the accretion flow, but the properties of the jet and their correlation with the accretion flow are not so well understood (Motta & Fender 2019). Since the X-ray PA is strongly

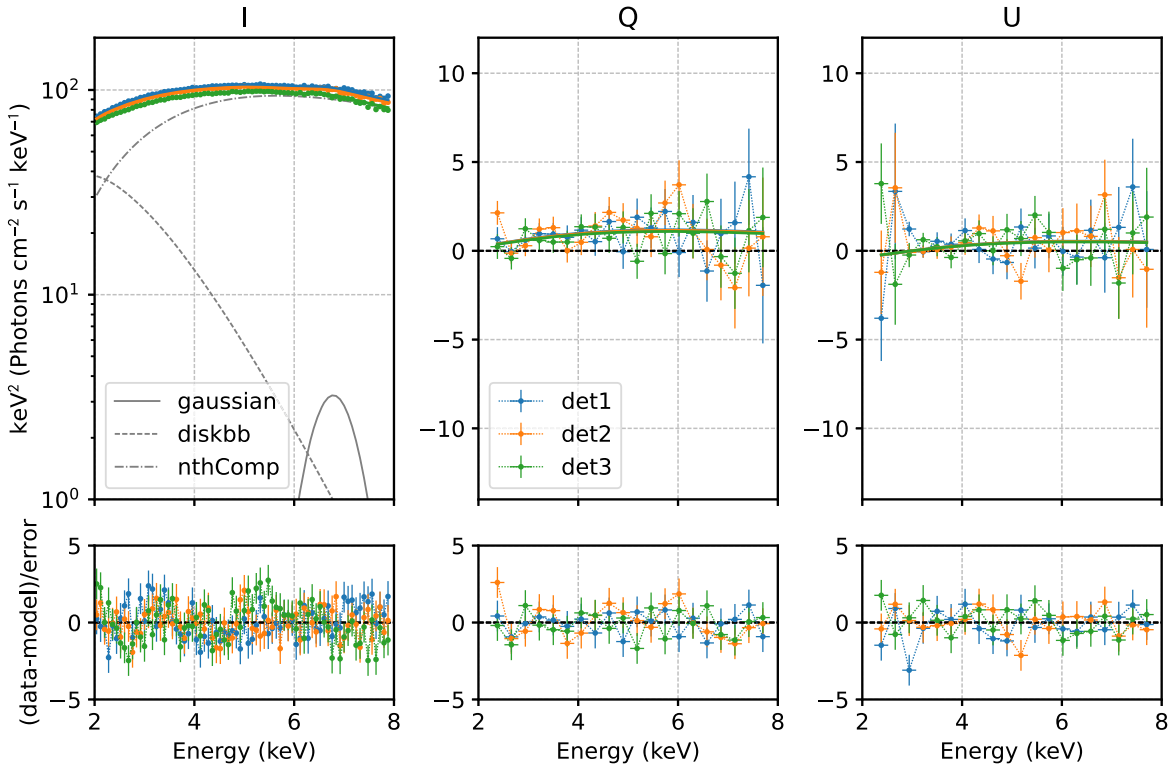

Figure 8. Spectral joint fit of the Stokes parameters I, Q, and U in EF_E representation in the 2–8 keV energy band using the three IXPE detectors and applying the model `tbabs*(gauss+polconst*diskbb+polconst*nthcomp)`. The best fit has $\chi^2/\mathrm{dof} = 1329/1337 = 0.99$. Energy rebinning is only for plotting purposes.

dependent on the geometry of the accretion flow, the correlation between the radio-jet position angle and the PA is of great interest. For example, a previous study of the polarization in Sco X-1, reported in Long et al. (2022), was interpreted as an indication of a Sco X-1 corona residing in a vertically extended BL/SL located between the inner disk and the NS. In fact, for this scenario, the X-ray PA is expected to be perpendicular to the disk and aligned with the system axis, as the radio jet is assumed to be. Similarly, the IXPE results obtained for Cyg X-2 (Farinelli et al. 2023) and in the stellar-mass BH Cyg X-1 (Krawczynski et al. 2022) show an indication of a PA aligned with the radio jet. In the measurements reported here, both the model-independent and spectropolarimetric analyses show a PA at $8° \pm 6°$ that is not aligned with the Sco X-1 radio jet, which is at $54° \pm 3°$. The resulting rotation of the PA with respect to the radio-jet position angle is $46° \pm 9°$, different from the previous indication of alignment between the PA and radio jet. However, none of these X-ray polarization measurements were performed simultaneously with the radio ones. The orientation of the jet in a few sources has been seen to change on short timescales (hours), as in the case of the BH system V404 Cygni (Miller-Jones et al. 2019), likely due to the Lense–Thirring precession of the accretion disk (Stella & Vietri 1998). Although not yet observed, this can also be expected for NSs, and the observed misalignment between the IXPE-measured PA and the radio jet (Fomalont et al. 2001b) could be consistent with this effect (e.g., the V404 Cygni rapid variation of the radio-jet position angle ranged from $-30\overset{\circ}{.}6$ to $+5\overset{\circ}{.}6$, that is, a 36° rotation).

This new result by IXPE is a strong improvement in terms of significance with respect to the two previous attempts to measure the X-ray polarization of Sco X-1. The first one was performed by OSO-8 (Long et al. 1979), and the second one was recently performed by PolarLight (Long et al. 2022). Neither of these attempts were performed with an instrument capable of performing spectral analysis; thus, it was not possible to identify the status of Sco X-1. Moreover, only upper limits or marginal detections were achieved. The OSO-8 PD is compatible within 1σ with the present ones of Table 2 at both 2.6 and 5.2 keV. The PA shows marginal variations with respect to this IXPE measurement at levels of $33° \pm 14°$ and $45° \pm 8°$ at 2.6 and 5.2 keV, respectively. PolarLight divided its data in two energy bins and two source flux states, low and high, on the basis of the measured count rate. For the low-flux state, PolarLight was capable of obtaining only upper limits in both energy bins that are compatible with the IXPE result. For the high-flux state, the 3–4 keV PD is still compatible, while the PA differs by $55° \pm 19°$; the 4–8 keV PD differs by $3.0\% \pm 0.8\%$, and the PA differs by $41° \pm 7°$. When PolarLight data are analyzed without any flux selection, the upper limit in 3–4 keV is compatible with the IXPE result, while the 4–8 keV values differ by $1.3\% \pm 0.6\%$ for the PD and $44° \pm 9°$ for the PA.

This comparison with previous observations, although without a clear state identification, in light of previous IXPE results for other Z-sources (Cocchi et al. 2023; Fabiani et al. 2023; Farinelli et al. 2023; Rankin et al. 2023), can allow for some considerations. In Cocchi et al. (2023), Fabiani et al. (2023), and Rankin et al. (2023), variations of the polarimetric properties along the Z-track are reported. The sources observed in the HB (Cocchi et al. 2023; Fabiani et al. 2023; Farinelli et al. 2023) showed a higher PD, in line with the result of PolarLight for the high flux (Long et al. 2022). Moreover, for

Cyg X-2 (Farinelli et al. 2023), the HB PA results to be aligned with the measured radio-jet direction. On the other hand, this Sco X-1 observation was dominated by the SA, where the flux is smaller, and this may correspond to the low-flux state in the PolarLight result, which is compatible, although with a much smaller significance, with the IXPE result. These considerations give an indication of a polarization variation along the Z-branches for Sco X-1 with an NB/HB state having higher polarization, at the level of the PolarLight result, and PA variations up to $\sim 50^{\circ}$, in line with other IXPE results (Cocchi et al. 2023; Rankin et al. 2023). IXPE's different measured PA with respect to the previous observations can be explained with a variation of the corona geometry in the different states of the source.

Because of these uncertainties on how the polarization changes along the Z-branches, it may be crucial to have new Sco X-1 observations, possibly coordinated with radio ones, to correlate the jet emission direction with the PA. This kind of study could be of great impact, allowing us to verify the impact of the Lense–Thirring precession and/or geometrical variations of the radio emissions with the corona geometry.

7. Summary

In this paper, we report the highly significant ($\sim 7\sigma$ CL) detection of polarization from Sco X-1 obtained by IXPE. During the IXPE observation, the source was observed mainly in the SA state. The spectral analysis has been performed using simultaneous NICER, NuSTAR, Insight-HXMT, and IXPE observations. The spectral model is described by `diskbb` to describe the direct disk or SL emission, `nthcomp` to describe the Comptonization component having blackbody seed photons emitted by the NS BL/SL, and a broad line at ~ 6.7 keV due to reflection (also, a more complex reflection model can be included). The reflection analysis by using the `relxillNS` model improves the reduced χ^2 and allows setting an upper limit on the inner disk radius of $\sim 2R_{\rm ISCO}$, compatible with a scenario with the disk close the NS surface. A PD at a level of 1% is measured, and a PA misalignment with respect to the direction of the radio jet, that, is 54° (north to east on the sky plane; Fomalont et al. 2001a, 2001b), is observed. A discrepancy between the IXPE results and the previous attempts by OSO-8 and PolarLight is also reported.

Polarization studies in other Z-sources, performed by IXPE (Cocchi et al. 2023; Fabiani et al. 2023; Rankin et al. 2023), showed polarization variations along the different states of the sources with PA changing up to $\sim 50^{\circ}$. This can explain these PA discrepancies in terms of changes of the Z-branch in which Sco X-1 was observed. In conclusion, these different PAs can indicate a corona geometry that changes along the Z-track. Alternatively, the IXPE PA misalignment with previous radio-jet direction measurements can be explained with relativistic precession that may have altered the radio-jet position.

Acknowledgments

The Imaging X-ray Polarimetry Explorer (IXPE) is a joint US and Italian mission. The US contribution is supported by the National Aeronautics and Space Administration (NASA) and led and managed by its Marshall Space Flight Center (MSFC), with industry partner Ball Aerospace (contract NNM15AA18C). The Italian contribution is supported by the Italian Space Agency (Agenzia Spaziale Italiana, ASI) through contract ASI-OHBI-2022-13-I.0, agreements ASI-INAF-2022-19-HH.0 and ASI-INFN-2017.13-H0, and its Space Science Data Center (SSDC) with agreements ASI-INAF-2022-14-HH.0 and ASI-INFN 2021-43-HH.0, and by the Istituto Nazionale di Astrofisica (INAF) and the Istituto Nazionale di Fisica Nucleare (INFN) in Italy. This research used data products provided by the IXPE Team (MSFC, SSDC, INAF, and INFN) and distributed with additional software tools by the High-Energy Astrophysics Science Archive Research Center (HEASARC) at NASA Goddard Space Flight Center (GSFC).

The authors acknowledge the NICER, NuSTAR, and Insight-HXMT teams for the prompt scheduling of the simultaneous observations. In particular, the authors acknowledge Karl Forster, Hannah Penn Earnshaw, Hiromasa Miyasaka, Murray Brightman, and Fiona A. Harrison.

We acknowledge support from Academy of Finland grants 333112, 349144, and 355672 (J.P., A.V., S.S.T.) and the German Academic Exchange Service (DAAD) travel grant 57525212 (V.D.). A.Pap., F.A., and G.I. are supported by INAF (research grant "Uncovering the optical beat of the fastest magnetized neutron stars (FANS)") and the Italian Ministry of University and Research (MUR; PRIN 2020, grant 2020BRP57Z, "Gravitational and Electromagnetic-wave Sources in the Universe with current and next-generation detectors (GEMS)"). F.X. is supported by the National Natural Science Foundation of China (grant No. 12373041). K.L. is supported by the National Natural Science Foundation of China (grant No. 12133003). F.X. and K.L. are supported by the National Key R&D Program of China (grant No. 2023YFE0117200). I.L. was supported by the NASA Postdoctoral Program at the Marshall Space Flight Center, administered by Oak Ridge Associated Universities under contract with NASA. P.O.P. acknowledges financial support from the French High Energy Program (PNHE/CNRS) and the French Space Agency (CNES).

Facilities: IXPE, NICER, NuSTAR, Insight-HXMT.

Software: IXPEOBSSIM (Baldini et al. 2022), XSPEC (Arnaud 1996), HEASOFT (Blackburn 1995), STINGRAY (Huppenkothen et al. 2019), HXMTDAS (Zhang et al. 2020).

Appendix
Data Handling for X-Ray Observatories

In the following subsections, we report how data were extracted and the software tools we used for the analysis of the data from X-ray observatories.

A.1. IXPE

The IXPE is a joint NASA and Italian Space Agency mission launched on 2021 December 9 and entirely dedicated to measuring linear X-ray polarization. The performance and an extensive description of the observatory are reported in Weisskopf et al. (2022). IXPE comprises three identical grazing incidence telescopes, providing imaging and spectral polarimetry over the 2–8 keV energy band with a time resolution of better than 15 μs. Each telescope couples an X-ray module of mirror assembly and a DU hosting a gas-pixel detector, which is a photoelectric polarimeter sensitive to linear X-ray polarization (Costa et al. 2001; Soffitta et al. 2021).

Thanks to its imaging capability, we selected the source photons from the IXPE telescope images inside a circular region of radius 100″ centered on the source position. No background regions were selected on the images, following the prescription reported in Di Marco et al. (2023b) for bright

sources with a high count rate ($\gtrsim$2 counts s^{-1}), which is the case for Sco X-1.

The IXPE data were processed using the `xpbin` tool in IXPEOBSSIM (Baldini et al. 2022) to obtain the Pulse Height Analyzer Stokes spectra for the spectropolarimetric analysis with XSPEC. All obtained spectra were grouped to have at least 50 counts bin^{-1}.

A.2. NICER

NICER, on board the International Space Station and launched in 2017 June, is a soft X-ray instrument consisting of 56 coaligned concentrator X-ray optics, each one having a single silicon drift detector in the focus (Gendreau et al. 2016). NICER does not offer imaging capabilities but has a large collecting area providing unmatched time resolution in the soft X-ray bandpass, with a sensitive energy interval of 0.2–12 keV. Contemporaneous observations of Sco X-1 during IXPE observation were performed in the framework of NICER GO Cycle 5 (proposal 6189).

The NICER data were processed with the NICER Data Analysis Software v010a released on 2022 December 16 and provided under HEASOFT v6.31.1, with the CALDB version released on 2022 October 30. The background spectra have been estimated by applying the new SCORPEON model. All obtained spectra were grouped to have at least 50 counts bin^{-1}.

A.3. NuSTAR

The NuSTAR observatory (Harrison et al. 2013) consists of two identical X-ray telescopes, referred to as FPMA and FPMB. They provide broadband X-ray imaging, spectroscopy, and timing in the energy range 3–79 keV with angular resolution of 18″ (FWHM) and spectral resolution of 400 eV (FWHM) at 10 keV. The NuSTAR observation was performed in the framework of NuSTAR GO Cycle 9 (proposal 9212).

The NuSTAR data were processed with the standard Data Analysis Software (`nustardas` 16Feb22 v2.1.2) provided under HEASOFT v6.31.1 with the CALDB version released on 2023 April 4 by using the `statusexpr="STATUS==b0000xxx00xxxx000"` keyword in the NUPIPELINE, as suggested for bright sources.[58] Both source and background regions are obtained by applying a circular 150″ radius selection; the spectra are extracted in these regions centered on the location of Sco X-1 for the source and, for the background, in an off-center sourceless region in the field of view. All obtained spectra were grouped to have at least 50 counts bin^{-1}.

A.4. Insight-HXMT

Insight-HXMT is the first Chinese X-ray satellite, launched in 2017 June (Zhang et al. 2014, 2020). The satellite comprises three different instruments: (i) the low-energy instrument, working in 1–15 keV and consisting of 96 swept charge devices, with an effective area of 384 cm^{-2}; (ii) the ME instrument, working in the 5–30 keV range and consisting of 1728 Si-Pin units, with an effective area of 952 cm^{-2}; and (iii) the HE instrument, working in 20–250 keV and consisting of 18 NaI(Ti)/CsI(Na) scintillation detectors, with an effective area of 5100 cm^{-2} (Li et al. 2020; Zhang et al. 2020).

The data reduction of Insight-HXMT was performed utilizing Insight-HXMT Data Analysis Software `HXMTDAS` v2.04 with default filter criteria, including an elevation angle of $>10°$; a geometric cutoff rigidity of >8 GeV, offset for the point position $\leqslant 0.°04$; and a time beyond 300 s to the South Atlantic Anomaly.

[58] https://heasarc.gsfc.nasa.gov/docs/nustar/analysis/

ORCID iDs

Fabio La Monaca https://orcid.org/0000-0001-8916-4156
Alessandro Di Marco https://orcid.org/0000-0003-0331-3259
Juri Poutanen https://orcid.org/0000-0002-0983-0049
Matteo Bachetti https://orcid.org/0000-0002-4576-9337
Sara Elisa Motta https://orcid.org/0000-0002-6154-5843
Alessandro Papitto https://orcid.org/0000-0001-6289-7413
Maura Pilia https://orcid.org/0000-0001-7397-8091
Fei Xie https://orcid.org/0000-0002-0105-5826
Stefano Bianchi https://orcid.org/0000-0002-4622-4240
Anna Bobrikova https://orcid.org/0009-0009-3183-9742
Enrico Costa https://orcid.org/0000-0003-4925-8523
Wei Deng https://orcid.org/0000-0002-9370-4079
Ming-Yu Ge https://orcid.org/0000-0002-3776-4536
Giulia Illiano https://orcid.org/0000-0003-4795-7072
Shu-Mei Jia https://orcid.org/0000-0002-5203-8321
Henric Krawczynski https://orcid.org/0000-0002-1084-6507
Eleonora Veronica Lai https://orcid.org/0000-0002-6421-2198
Kuan Liu https://orcid.org/0009-0007-8686-9012
Guglielmo Mastroserio https://orcid.org/0000-0003-4216-7936
Fabio Muleri https://orcid.org/0000-0003-3331-3794
John Rankin https://orcid.org/0000-0002-9774-0560
Paolo Soffitta https://orcid.org/0000-0002-7781-4104
Alexandra Veledina https://orcid.org/0000-0002-5767-7253
Filippo Ambrosino https://orcid.org/0000-0001-7915-996X
Melania Del Santo https://orcid.org/0000-0002-1793-1050
Wei Chen https://orcid.org/0000-0002-5965-7432
Javier A. Garcia https://orcid.org/0000-0003-3828-2448
Philip Kaaret https://orcid.org/0000-0002-3638-0637
Thomas D. Russell https://orcid.org/0000-0002-7930-2276
Wen-Hao Wei https://orcid.org/0009-0000-2414-9449
Shuang-Nan Zhang https://orcid.org/0000-0001-5586-1017
Chao Zuo https://orcid.org/0009-0007-5244-2379
Massimo Cocchi https://orcid.org/0000-0002-5817-3129
Andrea Gnarini https://orcid.org/0000-0002-0642-1135
Ruben Farinelli https://orcid.org/0000-0003-2212-367X
Keith Gendreau https://orcid.org/0000-0001-7115-2819
Francesco Ursini https://orcid.org/0000-0001-9442-7897
Martin C. Weisskopf https://orcid.org/0000-0002-5270-4240
Silvia Zane https://orcid.org/0000-0001-5326-880X
Iván Agudo https://orcid.org/0000-0002-3777-6182
Lucio A. Antonelli https://orcid.org/0000-0002-5037-9034
Luca Baldini https://orcid.org/0000-0002-9785-7726
Wayne H. Baumgartner https://orcid.org/0000-0002-5106-0463
Ronaldo Bellazzini https://orcid.org/0000-0002-2469-7063
Stephen D. Bongiorno https://orcid.org/0000-0002-0901-2097
Raffaella Bonino https://orcid.org/0000-0002-4264-1215
Alessandro Brez https://orcid.org/0000-0002-9460-1821

Niccolò Bucciantini https://orcid.org/0000-0002-8848-1392
Fiamma Capitanio https://orcid.org/0000-0002-6384-3027
Simone Castellano https://orcid.org/0000-0003-1111-4292
Elisabetta Cavazzuti https://orcid.org/0000-0001-7150-9638
Chien-Ting Chen https://orcid.org/0000-0002-4945-5079
Stefano Ciprini https://orcid.org/0000-0002-0712-2479
Alessandra De Rosa https://orcid.org/0000-0001-5668-6863
Ettore Del Monte https://orcid.org/0000-0002-3013-6334
Laura Di Gesu https://orcid.org/0000-0002-5614-5028
Niccolò Di Lalla https://orcid.org/0000-0002-7574-1298
Immacolata Donnarumma https://orcid.org/0000-0002-4700-4549
Victor Doroshenko https://orcid.org/0000-0001-8162-1105
Michal Dovčiak https://orcid.org/0000-0003-0079-1239
Steven R. Ehlert https://orcid.org/0000-0003-4420-2838
Teruaki Enoto https://orcid.org/0000-0003-1244-3100
Yuri Evangelista https://orcid.org/0000-0001-6096-6710
Sergio Fabiani https://orcid.org/0000-0003-1533-0283
Riccardo Ferrazzoli https://orcid.org/0000-0003-1074-8605
Shuichi Gunji https://orcid.org/0000-0002-5881-2445
Jeremy Heyl https://orcid.org/0000-0001-9739-367X
Wataru Iwakiri https://orcid.org/0000-0002-0207-9010
Svetlana G. Jorstad https://orcid.org/0000-0001-6158-1708
Vladimir Karas https://orcid.org/0000-0002-5760-0459
Fabian Kislat https://orcid.org/0000-0001-7477-0380
Jeffery J. Kolodziejczak https://orcid.org/0000-0002-0110-6136
Luca Latronico https://orcid.org/0000-0002-0984-1856
Ioannis Liodakis https://orcid.org/0000-0001-9200-4006
Simone Maldera https://orcid.org/0000-0002-0698-4421
Alberto Manfreda https://orcid.org/0000-0002-0998-4953
Frédéric Marin https://orcid.org/0000-0003-4952-0835
Andrea Marinucci https://orcid.org/0000-0002-2055-4946
Alan P. Marscher https://orcid.org/0000-0001-7396-3332
Herman L. Marshall https://orcid.org/0000-0002-6492-1293
Francesco Massaro https://orcid.org/0000-0002-1704-9850
Giorgio Matt https://orcid.org/0000-0002-2152-0916
Tsunefumi Mizuno https://orcid.org/0000-0001-7263-0296
Michela Negro https://orcid.org/0000-0002-6548-5622
Chi-Yung Ng https://orcid.org/0000-0002-5847-2612
Stephen L. O'Dell https://orcid.org/0000-0002-1868-8056
Nicola Omodei https://orcid.org/0000-0002-5448-7577
Chiara Oppedisano https://orcid.org/0000-0001-6194-4601
George G. Pavlov https://orcid.org/0000-0002-7481-5259
Abel L. Peirson https://orcid.org/0000-0001-6292-1911
Matteo Perri https://orcid.org/0000-0003-3613-4409
Melissa Pesce-Rollins https://orcid.org/0000-0003-1790-8018
Pierre-Olivier Petrucci https://orcid.org/0000-0001-6061-3480
Andrea Possenti https://orcid.org/0000-0001-5902-3731
Simonetta Puccetti https://orcid.org/0000-0002-2734-7835
Brian D. Ramsey https://orcid.org/0000-0003-1548-1524
Ajay Ratheesh https://orcid.org/0000-0003-0411-4243
Oliver J. Roberts https://orcid.org/0000-0002-7150-9061
Roger W. Romani https://orcid.org/0000-0001-6711-3286
Carmelo Sgrò https://orcid.org/0000-0001-5676-6214
Patrick Slane https://orcid.org/0000-0002-6986-6756
Gloria Spandre https://orcid.org/0000-0003-0802-3453
Douglas A. Swartz https://orcid.org/0000-0002-2954-4461
Toru Tamagawa https://orcid.org/0000-0002-8801-6263
Fabrizio Tavecchio https://orcid.org/0000-0003-0256-0995
Roberto Taverna https://orcid.org/0000-0002-1768-618X
Allyn F. Tennant https://orcid.org/0000-0002-9443-6774
Nicholas E. Thomas https://orcid.org/0000-0003-0411-4606
Francesco Tombesi https://orcid.org/0000-0002-6562-8654
Alessio Trois https://orcid.org/0000-0002-3180-6002
Sergey S. Tsygankov https://orcid.org/0000-0002-9679-0793
Roberto Turolla https://orcid.org/0000-0003-3977-8760
Jacco Vink https://orcid.org/0000-0002-4708-4219
Kinwah Wu https://orcid.org/0000-0002-7568-8765

References

Andrew, B. H., & Purton, C. R. 1968, Natur, 218, 855
Arnason, R. M., Papei, H., Barmby, P., Bahramian, A., & Gorski, M. D. 2021, MNRAS, 502, 5455
Arnaud, K. A. 1996, in ASP Conf. Ser. 101, Astronomical Data Analysis Software and Systems V, ed. G. H. Jacoby & J. Barnes (San Francisco, CA: ASP), 17
Bahramian, A., & Degenaar, N. 2023, in Handbook of X-ray and Gamma-ray Astrophysics, ed. C. Bambi & A. Santangelo (Berlin: Springer), 120
Baldini, L., Bucciantini, N., Lalla, N. D., et al. 2022, SoftX, 19, 101194
Barret, D., & Vaughan, S. 2012, ApJ, 746, 131
Bartlett, M. S. 1948, Natur, 161, 686
Blackburn, J. K. 1995, in ASP Conf. Ser. 77, Astronomical Data Analysis Software and Systems IV, ed. R. A. Shaw, H. E. Payne, & J. J. E. Hayes (San Francisco, CA: ASP), 367
Bradshaw, C. F., Fomalont, E. B., & Geldzahler, B. J. 1999, ApJL, 512, L121
Cackett, E. M., Miller, J. M., Ballantyne, D. R., et al. 2010, ApJ, 720, 205
Cackett, E. M., Miller, J. M., Bhattacharyya, S., et al. 2008, ApJ, 674, 415
Cackett, E. M., Miller, J. M., Reis, R. C., Fabian, A. C., & Barret, D. 2012, ApJ, 755, 27
Capitanio, F., Fabiani, S., Gnarini, A., et al. 2023, ApJ, 943, 129
Casella, P., Belloni, T., & Stella, L. 2006, A&A, 446, 579
Chandrasekhar, S. 1960, Radiative Transfer (New York: Dover)
Chatterjee, R., Agrawal, V. K., Jayasurya, K. M., & Katoch, T. 2023, MNRAS, 521, L74
Churazov, E., Sunyaev, R., & Sazonov, S. 2002, MNRAS, 330, 817
Church, M. J., Gibiec, A., Bałucińska-Church, M., & Jackson, N. K. 2012, A&A, 546, A35
Cocchi, M., Gnarini, A., Fabiani, S., et al. 2023, A&A, 674, L10
Costa, E., Soffitta, P., Bellazzini, R., et al. 2001, Natur, 411, 662
Coughenour, B. M., Cackett, E. M., Miller, J. M., & Ludlam, R. M. 2018, ApJ, 867, 64
Di Marco, A., Costa, E., Muleri, F., et al. 2022a, AJ, 163, 170
Di Marco, A., Muleri, F., Fabiani, S., et al. 2022b, Proc. SPIE, 12181, 121811C
Di Marco, A., La Monaca, F., Poutanen, J., et al. 2023a, ApJL, 953, L22
Di Marco, A., Soffitta, P., Costa, E., et al. 2023b, AJ, 165, 143
Dickey, J. M., & Lockman, F. J. 1990, ARA&A, 28, 215
Ding, G. Q., Qu, J. L., Song, L. M., et al. 2023, ApJ, 950, 69
Fabian, A. C., Rees, M. J., Stella, L., & White, N. E. 1989, MNRAS, 238, 729
Fabiani, S., Capitanio, F., Iaria, R., et al. 2023, A&A, submitted, arXiv:2310.06788
Farinelli, R., Fabiani, S., Poutanen, J., et al. 2023, MNRAS, 519, 3681
Ferrazzoli, R., Muleri, F., Lefevre, C., et al. 2020, JATIS, 6, 048002
Fomalont, E. B., Geldzahler, B. J., & Bradshaw, C. F. 2001a, ApJL, 553, L27
Fomalont, E. B., Geldzahler, B. J., & Bradshaw, C. F. 2001b, ApJ, 558, 283
Galloway, D. K., Premachandra, S., Steeghs, D., et al. 2014, ApJ, 781, 14
García, J. A., Dauser, T., Ludlam, R., et al. 2022, ApJ, 926, 13
Gendreau, K. C., Arzoumanian, Z., Adkins, P. W., et al. 2016, Proc. SPIE, 9905, 99051H
Giacconi, R., Gursky, H., Paolini, F. R., & Rossi, B. B. 1962, PhRvL, 9, 439
Gilfanov, M., Revnivtsev, M., & Molkov, S. 2003, A&A, 410, 217
Gnarini, A., Ursini, F., Matt, G., et al. 2022, MNRAS, 514, 2561
Gottlieb, E. W., Wright, E. L., & Liller, W. 1975, ApJL, 195, L33
Grefenstette, B., Brightman, M., Earnshaw, H. P., et al. 2022, arXiv:2206.04058

HI4PI Collaboration, Ben Bekhti, N., Flöer, L., et al. 2016, A&A, 594, A116
Haardt, F., & Matt, G. 1993, MNRAS, 261, 346
Harrison, F. A., Craig, W. W., Christensen, F. E., et al. 2013, ApJ, 770, 103
Hasinger, G., & van der Klis, M. 1989, A&A, 225, 79
Huppenkothen, D., Bachetti, M., Stevens, A. L., et al. 2019, ApJ, 881, 39
Inogamov, N. A., & Sunyaev, R. A. 1999, AstL, 25, 269
Jayasurya, K. M., Agrawal, V. K., & Chatterjee, R. 2023, MNRAS, 525, 4657
Kalberla, P. M. W., Burton, W. B., Hartmann, D., et al. 2005, A&A, 440, 775
Kislat, F., Clark, B., Beilicke, M., & Krawczynski, H. 2015, APh, 68, 45
Krawczynski, H., Muleri, F., Dovčiak, M., et al. 2022, Sci, 378, 650
Kuulkers, E., van der Klis, M., Oosterbroek, T., et al. 1994, A&A, 289, 795
Kuulkers, E., van der Klis, M., Oosterbroek, T., van Paradijs, J., & Lewin, W. H. G. 1997, MNRAS, 287, 495
Lapidus, I. I., & Sunyaev, R. A. 1985, MNRAS, 217, 291
Leahy, D. A., Darbro, W., Elsner, R. F., et al. 1983, ApJ, 266, 160
Li, X., Li, X., Tan, Y., et al. 2020, JHEAp, 27, 64
Long, K. S., Chanan, G. A., Ku, W. H. M., & Novick, R. 1979, ApJL, 232, L107
Long, X., Feng, H., Li, H., et al. 2022, ApJL, 924, L13
Loskutov, V. M., & Sobolev, V. V. 1982, Afz, 18, 81
Ludlam, R. M., Cackett, E. M., García, J. A., et al. 2022, ApJ, 927, 112
Ludlam, R. M., Miller, J. M., Arzoumanian, Z., et al. 2018, ApJL, 858, L5
Madsen, K. K., Forster, K., Grefenstette, B., Harrison, F. A., & Miyasaka, H. 2022, JATIS, 8, 034003
Matt, G. 1993, MNRAS, 260, 663
Matt, G. 2006, AN, 327, 949
Mazzola, S. M., Iaria, R., Di Salvo, T., et al. 2021, A&A, 654, A102
Miller-Jones, J. C. A., Tetarenko, A. J., Sivakoff, G. R., et al. 2019, Natur, 569, 374
Mondal, A. S., Dewangan, G. C., & Raychaudhuri, B. 2020, MNRAS, 494, 3177
Mondal, A. S., Raychaudhuri, B., Dewangan, G. C., & Beri, A. 2022, MNRAS, 516, 1256
Motta, S. E., & Fender, R. P. 2019, MNRAS, 483, 3686
Popham, R., & Sunyaev, R. 2001, ApJ, 547, 355
Poutanen, J., Nagendra, K. N., & Svensson, R. 1996, MNRAS, 283, 892
Poutanen, J., & Svensson, R. 1996, ApJ, 470, 249
Poutanen, J., Veledina, A., & Beloborodov, A. M. 2023, ApJL, 949, L10
Poutanen, J., & Vilhu, O. 1993, A&A, 275, 337
Psaltis, D., Lamb, F. K., & Miller, G. S. 1995, ApJL, 454, L137
Rankin, J., La Monaca, F., Di Marco, A., et al. 2023, ApJL, submitted, (arXiv:2311.04632)
Rankin, J., Muleri, F., Ferrazzoli, R., et al. 2023, Proc. SPIE, 12678, 126780D
Revnivtsev, M. G., & Gilfanov, M. R. 2006, A&A, 453, 253
Revnivtsev, M. G., Suleimanov, V. F., & Poutanen, J. 2013, MNRAS, 434, 2355
Schnittman, J. D., & Krolik, J. H. 2010, ApJ, 712, 908
Schulz, N. S., & Wijers, R. A. M. J. 1993, A&A, 273, 123
Shakura, N. I., & Sunyaev, R. A. 1988, AdSpR, 8, 135
Sobolev, V. V. 1963, A Treatise on Radiative Transfer (Princeton, NJ: Van Nostrand)
Soffitta, P., Baldini, L., Bellazzini, R., et al. 2021, AJ, 162, 208
Steeghs, D., & Casares, J. 2002, ApJ, 568, 273
Stella, L., & Vietri, M. 1998, ApJL, 492, L59
Suleimanov, V., & Poutanen, J. 2006, MNRAS, 369, 2036
Sunyaev, R. A., & Titarchuk, L. G. 1985, A&A, 143, 374
Titarchuk, L., Seifina, E., & Shrader, C. 2014, ApJ, 789, 98
Tomsick, J. A., Parker, M. L., Garcìa, J. A., et al. 2023, ApJ, 855, 3
Ursini, F., Farinelli, R., Gnarini, A., et al. 2023, A&A, 676, A20
van der Klis, M. 1989, ARA&A, 27, 517
Veledina, A., Muleri, F., Dovciak, M., et al. 2023, ApJL, 958, L16
Weisskopf, M. C., Soffitta, P., Baldini, L., et al. 2022, JATIS, 8, 026002
Wilkins, D. R. 2018, MNRAS, 475, 748
Wilms, J., Allen, A., & McCray, R. 2000, ApJ, 542, 914
Zdziarski, A. A., Johnson, W. N., & Magdziarz, P. 1996, MNRAS, 283, 193
Zhang, S., Lu, F. J., Zhang, S. N., & Li, T. P. 2014, Proc. SPIE, 9144, 914421
Zhang, S.-N., Li, T., Lu, F., et al. 2020, SCPMA, 63, 249502
Życki, P. T., Done, C., & Smith, D. A. 1999, MNRAS, 309, 561